Validation of Surface Current Measurements in the Northern Adriatic Sea from High-Frequency Radars

SIMONE COSOLI

Istituto Nazionale di Oceanografia e di Geofisica Sperimentale (OGS), Sgonico, Italy

ANDREA MAZZOLDI

Istituto di Scienze Marine, CNR, Venezia, Italy

MIROSLAV GAČIĆ

Istituto Nazionale di Oceanografia e di Geofisica Sperimentale (OGS), Sgonico, Italy

(Manuscript received 1 December 2008, in final form 9 December 2009)

ABSTRACT

The performances of a shore-based high-frequency (HF) radar network deployed along the coast of the Venice lagoon (northern Adriatic Sea) are discussed based on a comparison with a single bottom-mounted ADCP deployed in the shallow-water area offshore of the lagoon for a 40-day period in August–September 2005.

The analyses, carried out using currents representative of the first meter for the HF radars and 2.5 m for the ADCP, gave rms differences of radial currents in the range of 8.7–14.7 cm s^{-1} (correlation 0.37– 0.82) for the ideal pattern and 8.4–20.5 cm s^{-1} (correlation 0.14–0.84) for the measured pattern. Good correlation was found between surface current vectors and moored data (scalar correlation up to $R = 0.83$, vector correlation $\rho = 0.78$, veering angle 6°). Comparison metrics were improved for the low-passed currents. Angular offsets ranged between +6° and +11°. Differences depended primarily on the geophysical variability within the water column. Bearing offsets also contributed because they lead to comparisons with radial velocities at erroneous angular sectors.

Radar performances were severely affected by strong northeasterly wind pulses in their early stages. An increased broadband noise, spread over the entire Doppler spectrum across all ranges to the antennas, masked the Bragg peaks and determined the loss in radar coverage, introducing gross underestimations of both radial velocities and total currents.

1. Introduction

In recent years, there has been a constantly increasing interest in the development of high-frequency (HF) radars for the study of coastal circulation processes. Parallel to the development of reliable and cost-affordable instruments, interest also developed in error estimates and data reliability assessment. Error sources in HF radar–derived current estimates are varied, as might be expected for any remotely sensed measurement technique and include, among others, radio-wave interferences, reflections from moving ships, improper determination of the angle of arrival, and wide-area averaging. Many field studies performed comparisons with in situ observations, investigated uncertainties in HF radar measurements, and related them to either the sampling strategies or the geophysical processes in the area (Chapman et al. 1997; Graber et al. 1997; Cosoli et al. 2005). Typical uncertainties derived from investigations on current vectors or at a level of radial velocities (Emery et al. 2004) range between 8 and 12 cm s^{-1}.

There are various reasons for a new study on the accuracy of surface current measurements from HF radars—for instance, the oceanographic settings in which the radars operated during the experiment and the locations chosen for the antennas. The northern Adriatic Sea is a shallow-water semi-enclosed basin, with depth within

Corresponding author address: Simone Cosoli, Istituto Nazionale di Oceanografia e di Geofisica Sperimentale (OGS), Sgonico, TS, Italy.
E-mail: scosoli@ogs.trieste.it

DOI: 10.1175/2009JTECHO680.1

the radar domain ranging between 2 and 20 m in its deepest location. Waves are low and currents are weak because the typical magnitudes for surface flow are comparable to the uncertainty levels of the radar themselves. At the same time, they exhibit a large variability under the passage of meteorological fronts that enhance or invert the local circulation patterns (Kovačević et al. 2004; Gačić et al. 2009), and build up significant waves (Cavaleri et al. 1997). It presents a marked seasonal vertical stratification that forces density-driven flow (Cushman-Roisin et al. 2001; Bergamasco et al. 1996). Antennas are installed in densely inhabited areas with a number of potential sources of electromagnetic interferences, or surrounded by metal structures in the antenna near field. A new compact collocated transmit-and-receive antenna specifically developed was deployed and tested, which increased the previously investigated area (Kovačević et al. 2004).

Rather than proposing an exhaustive investigation of the interfering sources, which is beyond the scope of the present work, this paper evaluates radar capabilities at a level of radial velocities for each station for both the ideal and measured antenna beam patterns. The investigations are then complemented with a comparison of surface current vectors and moored velocities. Results of the present analyses show that a large fraction of the differences with moored currents can be explained in terms of geophysical processes occurring within the water column. Bearing offsets originating either from beam pattern distortions or pattern oversmoothing also contribute to differences with moored velocities. Their effects, however, are limited to the radial components and affect, to a minor extent, the accuracy of surface currents. Independently of their operating frequencies, radars are also shown to suffer from strong wind pulses, typically occurring during winter seasons, which limit spatial coverage and determine significant underestimations of current speed.

The paper is organized as follows: the experimental setup is given in section 2; section 3 describes the analysis methods; section 4 and section 5 report on the comparison of radial currents; section 6 focuses on the total current vectors; and sections 7 and 8 present the discussion of the results and the conclusions, respectively.

2. Experimental setup

A network of Coastal Ocean Dynamics Application Radar (CODAR) SeaSonde high-frequency radars are operated along the Venice lagoon littoral in the northern Adriatic Sea for the period 2001–06. Radars were installed with the primary purpose of monitoring surface currents in the area and studying dynamical features over a variety of sea conditions and time scales (Kovačević et al. 2004; Gačić et al. 2009). Two stations (Lido, Pellestrina, or Pele; see Fig. 1) consisted of separate transmit-and-receive antennas transmitting at 35.92 and 24.53 MHz with 150- and 200-kHz bandwidths (spatial resolution 1.0, 0.750 km, respectively), and a 1° angular resolution. A third station, consisting of a combined transmit-and-receive unit, was located on top of the oceanographic tower (Ptfv or tower site, Fig. 1), and transmitted at 24.90 MHz with a 150-kHz bandwidth and a 1° angular resolution. With respect to the two-antenna configuration described in Kovačević et al. (2004), the third station extended the investigated area to the three Venice lagoon inlets, where concurrent measurements of water flow exchange rates were conducted (Gačić et al. 2004). Radars were setup to produce hourly radial maps with both the ideal and measured antenna beam patterns. Surface current maps were derived following the least squares method proposed by Gurgel (1994) on a regular grid having 1 km $\times$ 1 km horizontal resolution using a 1.5-km search radius. Current vectors for poorly constrained grid points were removed, and time series for each grid point were quality-controlled and despiked following Kovačević et al. (2004).

A single bottom-mounted upward-looking 600-kHz ADCP current meter was deployed in the area adjacent to the lagoon littoral (Fig. 1) at 16-m depth. The current meter provided records of subsurface currents with a 50-cm vertical resolution and a 10-min resolution in time. Hourly averages of current speed and direction at each level were derived following a vector-averaging technique as averages of seven consecutive 10-min observations. The averaging process was centered at the cardinal hour to match the radar processing scheme as closely as possible. Subsurface hourly current records at the nominal depth of 2.5 m from the surface were then used for the subsequent comparison. Radars operated with the three-site configuration for the period January 2005–December 2006, whereas the ADCP was deployed for a 40-day period between August and October 2005. Thus, the comparison is limited to the period of common overlap.

Wind records and wave data (maximum H_m and significant H_s wave height, maximum and zero up-crossing period) were available from the oceanographic tower where the third radar was installed. Wind stress was derived following the Large and Pond (1981) formulation after reducing the hourly-averaged data to the standard 10-m height.

3. Analysis methods

Radars measure radial currents—that is, the component of sea surface currents moving radially with respect

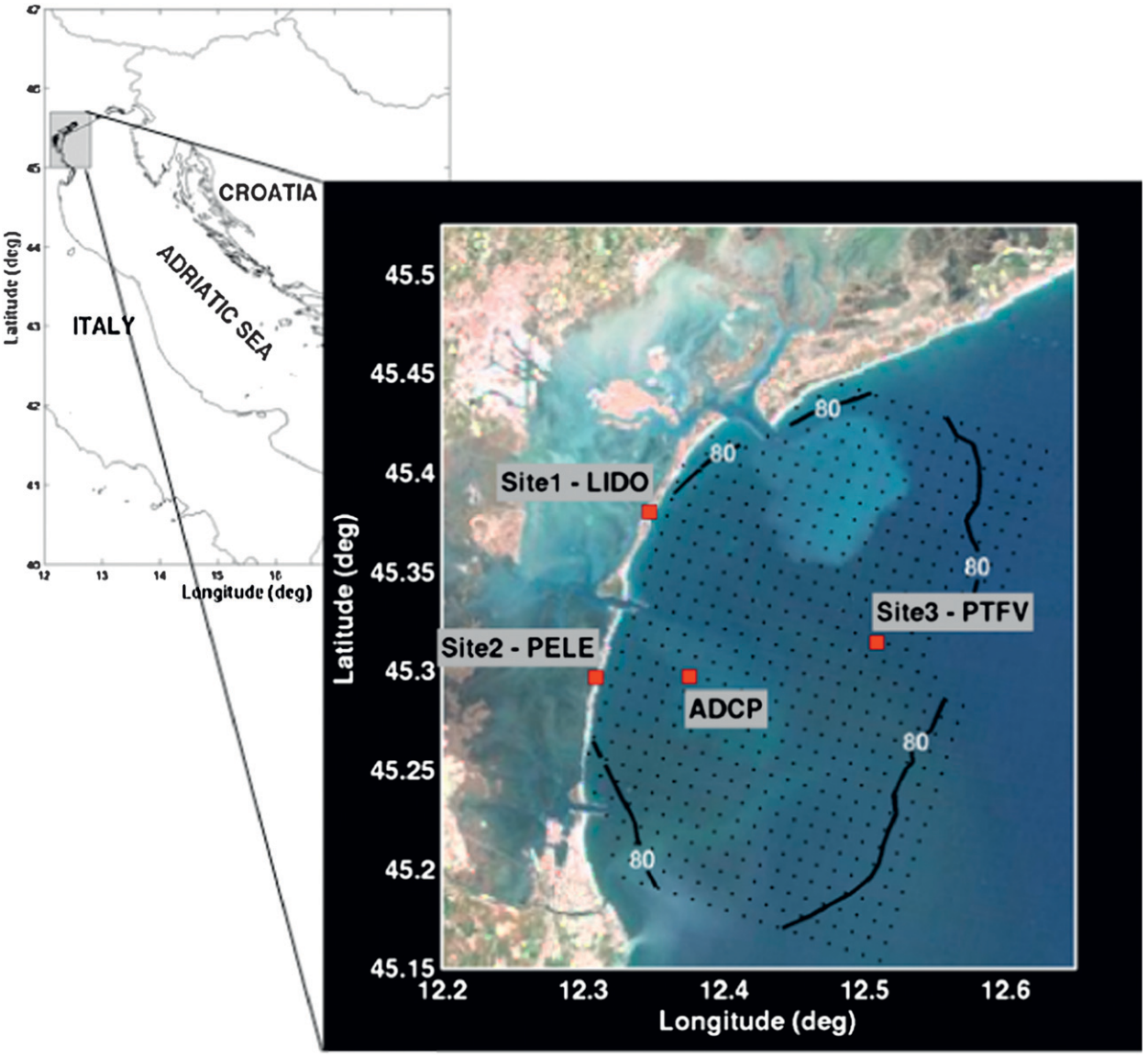

FIG. 1. Image of the study area showing the locations of the HF radars and the current meter. The 80% data return contour line is displayed, overlapped to the grid where currents are calculated.

to the antenna—whereas current meters measure the zonal (E–W) and the meridional (N–S) current components in a Cartesian reference frame. To compare radar radial currents V_{hf} to subsurface records, the moored current velocity vector is projected in the direction of a radar site:

$$V_m = U\cos\alpha + V\sin\alpha, \tag{1}$$

where α is the angle of the mooring with respect to the radar site; V_m is the radial component of moored currents; and U and V are the zonal and meridional components of subsurface currents, respectively. A time series of V_m, V_{hf}, and their differences are investigated by means of an appropriate set of statistical descriptors (correlation coefficient, root-mean-square values, mean, median, slope a and intercept b of the linear regression curve: $V_{\mathrm{hf}} = a\,V_m + b$).

To test for the presence of bearing offsets, which typically affect direction-finding (DF) radars such as the SeaSonde, correlation and rms differences are computed between V_m and V_{hf} using radial velocities at a fixed range and all angles. In the presence of bearing offsets, the angle that maximizes correlation and minimizes rms differences does not coincide with the angular sector containing the mooring. Following Emery et al. (2004), the bearing offset is thus expressed as

$$\Delta\theta = \theta_{\mathrm{exp}} - \theta_{\mathrm{max}}, \tag{2}$$

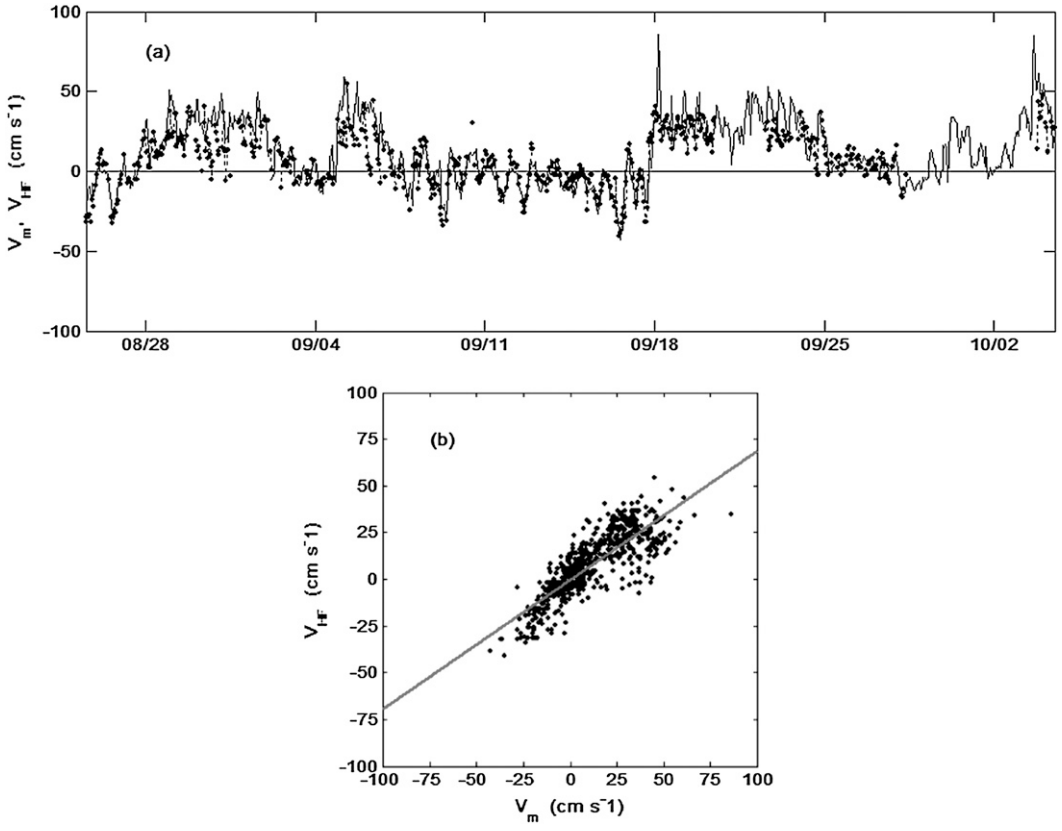

FIG. 2. Time series plot and scatter diagram of the radial velocities for the investigated period at the angle closest to the ADCP mooring for the LIDO radar station. The solid line corresponds to the ADCP data and dots correspond to radar radial velocities. Units are in cm s^{-1}.

where θ_{exp} is the bearing angle closest in angle to the mooring, and θ_{max} is the angle that optimizes the statistics. Positive (negative) values for the angular offset indicate that the maximum correlation sector is displaced clockwise (counterclockwise) from the sector containing the mooring. The statistical significance of pointing errors is then assessed by the comparison of the analysis results for radial velocities at θ_{max} and θ_{exp}.

4. Results: Radial velocities comparison

Both ideal and measured pattern radials V_{hf} at the angular sector closest to the ADCP mooring have gaps in time due to power interruptions, interferences, poor signal-to-noise conditions, or problems in determining a solution for the bearing angle (Paduan and Rosenfeld 1996). The typical gap duration is 2–3 h; longer gaps (2–5 days) are present at site 1 (Lido; Fig. 2) and site 3 (Ptfv or Tower), whereas site 2 (Pele) exhibits a more continuous coverage.

In general, radar radial velocities V_{hf} follow to a good extent moored radial velocities V_m. At Lido [range to the ADCP 9.5 km, bearing 166° measured clockwise from north (NCW)], V_{hf} exhibits a diurnal and semidiurnal variability, modulated by energetic forcing in the low-frequency band. At the Pellestrina site (range to the ADCP 5.2 km, bearing 89°NCW), radial currents have a lower range of variability and are dominated by diurnal forcing, modulated by a weaker low-frequency component. The different behavior of Lido and Pellestrina is related to the location of the current meter with respect to the radar sites. The radar-look direction for Lido was nearly parallel to the orientation of the mean flow, which presented a dominant low-frequency cyclonic circulation pattern (Kovačević et al. 2004; see also Fig. 3). The radar-look direction for Pele was, on the contrary, nearly perpendicular to the mean flow direction, which had a transversal component negligible with respect to that of tidal oscillations.

The statistical comparison of the radial velocities obtained from ideal and measured patterns for the three sites is presented in Table 1. Correlation coefficients of V_{hf} for the ideal pattern and V_m are $R = [0.82, 0.59]$ for Lido and Pellestrina sites (rms differences 12 and 8.68 cm s^{-1}). Slopes and intercepts of the least squares fit are $a = [0.69, 0.50]$, $b = [-0.24, -2]$ cm s^{-1}, respectively. Differences between V_m and V_{hf} are generally

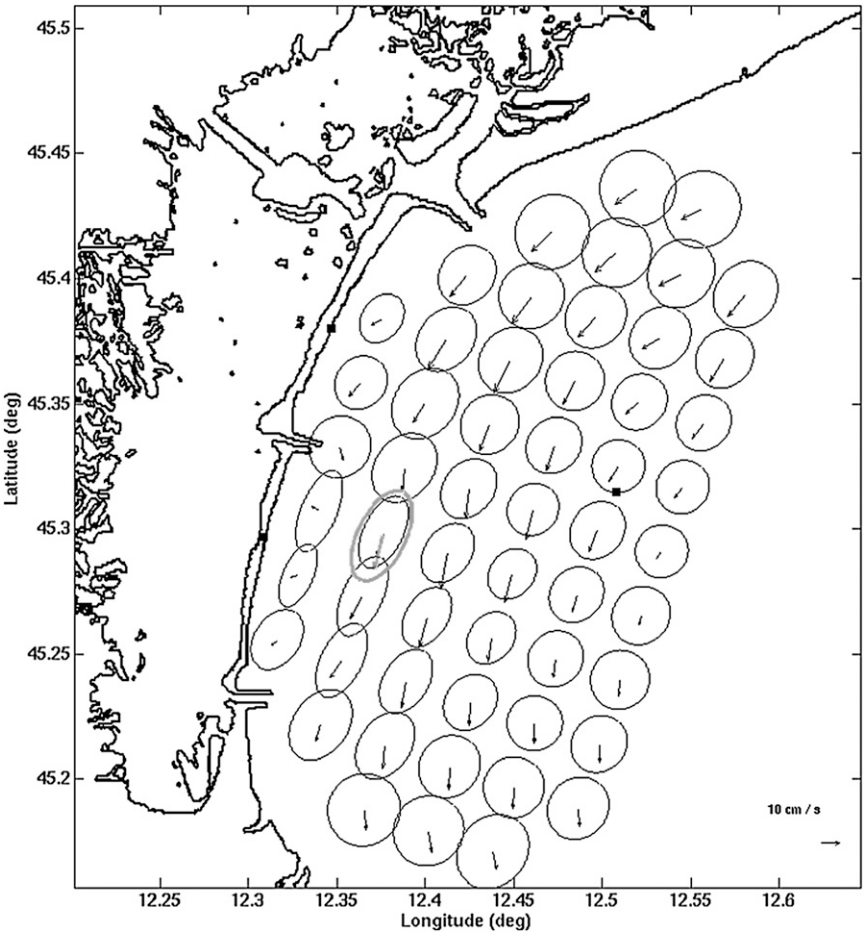

FIG. 3. Time-averaged currents and variance ellipses for surface (black curves) and subsurface (gray curve) currents. The surface flow pattern was subsampled to 6-km resolution for clarity.

small, with median values of 2 and a 3.8 cm s^{-1} mean bias, despite a 35 cm s^{-1} offset between the radial velocity maxima at Lido, and become negligible at Pellestrina (median value 0.06 cm s^{-1}, bias 0.21 cm s^{-1}).

Statistics improve at both sites for the measured pattern radials. Lido shows higher correlation and smaller differences, an increase in the slope, and a decrease in the intercept values ($R = 0.8$, rms difference 11.4 cm s^{-1}, 3 cm s^{-1} bias on the mean, median difference 1.21 cm s^{-1}, slope $a = 0.76$, intercept $b = 0.0089$ cm s^{-1}). Pellestrina also shows an increased correlation and slope as well as a small decrease in rms differences ($R = 0.66$, rms difference 8.08 cm s^{-1}, slope $a = 0.59$, intercept $b = -1.75$ cm s^{-1}). As for the ideal pattern, differences between V_{hf} and V_m are negligible (mean bias <0.1 cm s^{-1}, median difference <0.5 cm s^{-1}).

A lower agreement between V_{hf} and V_m characterizes the third site (range to the ADCP 10.6 km, bearing 259°NCW).

TABLE 1. Summary of the statistical comparison between the HF radar sites and the moored current meter.

Site	Pattern	Data points (h)	R	rms ΔV (cm s^{-1})	Bias (cm s^{-1})	
					Mean	Median
Lido	Ideal	626	0.824	12	3.83	1.87
	Measured	557	0.845	11.4	3.04	1.21
Pele	Ideal	865	0.5987	8.68	−0.21	0.06
	Measured	940	0.664	8.08	−0.08	−0.3
PTFV	Ideal	489	0.3767	14.7	2.7	1.94
	Measured	786	0.138	17.7	7.86	6.47

TABLE 2. Summary of the bearing offset estimates and the least squares fit parameters.

Site	Pattern	Bearing	R	Slope	95% CL	Intercept	95% CL
Lido	Ideal	−78°	0.824	0.693	[.6290, 0.7304]	−0.24	[−1.1126, 0.6555]
		−84°	0.83	0.733	[.6946, 0.7716]	−1.03	[−1.9, −0.1683]
	Measured	−78°	0.845	0.765	[.7252, 0.8058]	0.0089	[−.9626, 0.9805]
Pele	Ideal	+1	0.5987	0.5018	[.457, 0.5647]	−2.05	[−2.5575, −1.5409]
		+10	0.6882	0.6546	[.6098, 0.6993]	−2.687	[−3.1961, −2.1778]
	Measured	+1	0.664	0.5981	[.5549, 0.6412]	−1.7565	[−2.243, −1.2701]
		+7	0.6979	0.7626	[.6854, 0.8397]	−1.9226	[−2.7264, −1.1188]
Ptfv	Ideal	+191	0.3767	0.4619	[.3608, 0.5630]	1.4397	[.0318, 2.8476]
		+202	0.5858	0.8786	[.7787, 0.9784]	7.31	[5.85, 8.77]
	Measured	+191	0.138	0.1418	[.0704, 0.2131]	−1.8576	[−2.84, −0.8723]
		+201	0.50	0.8089	[.7035, 0.9143]	6.18	[4.7070, 7.6575]

Both the ideal and measured pattern radials have lower correlations (R = [0.37, 0.14]) and exhibit larger rms differences (14.7, 17.7 cm s^{-1}). Mean biases are 2.8 and 7.8 cm s^{-1}, and median differences are 2 and 6.5 cm s^{-1}; slopes and intercept values of the regression line are a = [0.46, 0.14] and b = [1.4, −0.18] cm s^{-1} for the ideal and measured patterns, respectively.

5. Results: Bearing offsets

As evident from Table 2, which presents the statistics (correlation coefficients, slopes, and intercept values) for radial velocities $V_{\rm hf}$ at $\theta_{\rm exp}$ and $\theta_{\rm max}$ [Eq. (2)] derived from the pointing error analysis, bearing offsets characterize at least two of three radars for the ideal and measured antenna patterns.

The +6° angular offset for the ideal pattern radials at Lido (Table 2) is not statistically significant because the distribution of the correlation coefficient around $\theta_{\rm exp}$ is flat and spans a large angular sector surrounding the mooring (Fig. 4). Both the mean bias and the median difference do not change at the two angles ($\theta_{\rm exp}$, $\theta_{\rm max}$). Furthermore, the increase in the slope of the regression line is not statistically significant at the 95% confidence level (CL), despite a significant increase in the intercept (b = 1.03 cm s^{-1}).

Pellestrina presents statistically significant bearing offsets for both the ideal and the measured pattern radials. The maximum correlation and minimum rms differences between V_m and $V_{\rm hf}$ for the ideal pattern are displaced 10° clockwise from the mooring. The larger correlation and lower rms differences (R = 0.68, rms differences 8.1 cm s^{-1}, number of hourly values N = 929 h) are accompanied by a significant improvement in both the slope and intercept values (a = 0.65, b = −2.68 cm s^{-1}) of the regression line. The angular displacement reduces to +6° for the measured antenna pattern.

The Ptfv site exhibits the largest bearing offsets for both the ideal ($\Delta\theta$ = +11°) and the measured ($\Delta\theta$ = +10°) patterns and the poorest agreement with the moored radial velocities at the mooring sector. Statistical analyses of $V_{\rm hf}$ versus V_m at $\theta_{\rm max}$ (Table 2) reveal an improvement of correlation coefficients (R = 0.58, 0.50), regression slopes (a = 0.87, 0.80), and intercept values (b = 7.31, 6.18 cm s^{-1}), along with a concurrent increase of the mean bias and the median difference (mean bias −6.2 cm s^{-1}, median difference −6 cm s^{-1}; the negative sign staying for $V_{\rm hf}$ velocities larger on average than V_m).

6. Results: Total vectors

With respect to radial currents, total vectors have a smaller amount of gaps because the vector computation takes advantage of radial velocities from several sectors surrounding the grid point.

Rotary spectra of surface currents, moored records, and wind stress at the tower are presented in Fig. 5. Surface radar currents have slightly more energy than moored data in the entire frequency spectrum but well capture the dominant spectral features of subsurface currents, in particular within the semidiurnal and diurnal tidal band. Both records show a polarization of the low-frequency subinertial frequencies with almost one order of magnitude more energy in the cyclonic spectrum (counterclockwise fluctuations) and a polarization in the antyciclonic spectrum at the inertial frequency.

The zonal and meridional components of surface currents (U, V) track subsurface components fairly well. The scalar correlation coefficient is R = [0.63, 0.81], rms differences are 8.22 and 12.6 cm s^{-1}, mean biases are lower than 1 and 4 cm s^{-1}, and the median differences are close to zero (−0.16 cm s^{-1}) for the U component and are below 2 cm s^{-1} for the V component. The magnitude of the vector correlation is ρ = 0.78, with a 6° veering angle, meaning that subsurface currents are on average 6° to the right of surface currents. After removing the high-frequency ''noise'' with a low-pass filter

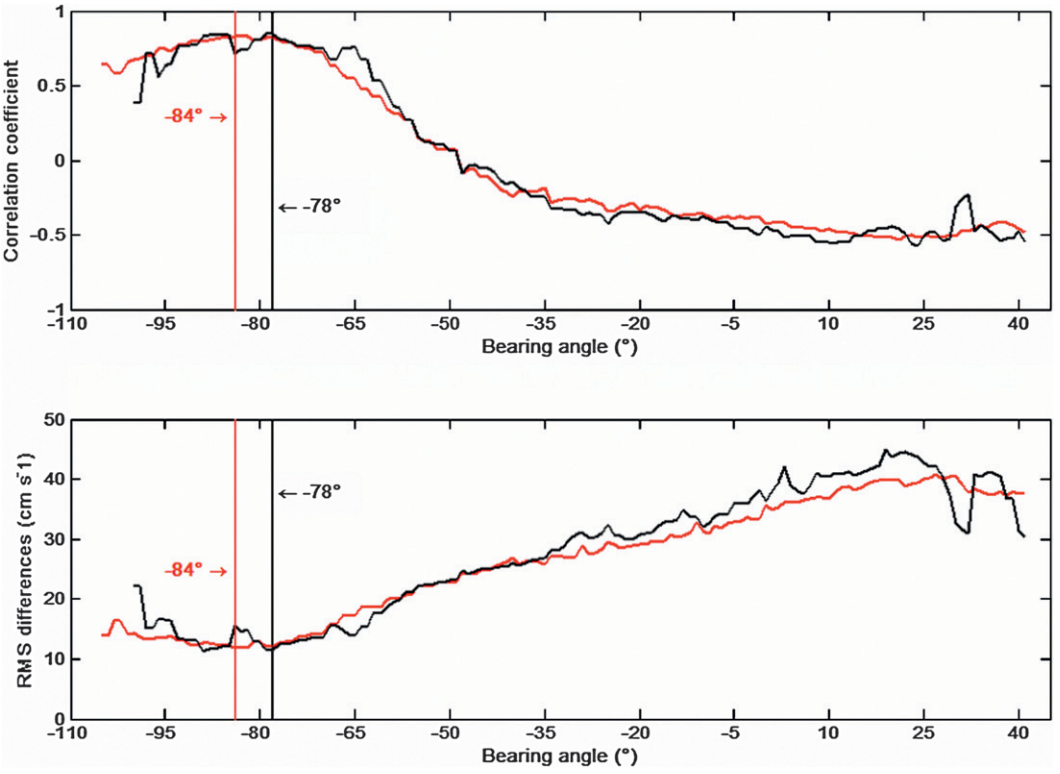

FIG. 4. (top) Angular evolution of correlation coefficient and (bottom) rms differences between radial currents at the LIDO site. The vertical lines denote the angles at which correlation between radial velocities is maximum, the corresponding angles are also evidenced. The red line refers to the ideal antenna beam pattern, and the black line corresponds to the measured antenna pattern. Units for rms differences are in cm s^{-1}.

[cut-off frequency $\omega = 0.03$ cycles per hour (cph)], the scalar correlations increase to $R = 0.76$, $R = 0.95$, while rms differences decrease to 3.8 and 6.85 cm s^{-1} for the U and V components, respectively. Vector correlation increases to $\rho = 0.96$, the angular offset decreases to 4°, and up to 73% of the instantaneous angles between current vectors are clustered in the range of $[-4°, +11°]$. Maximum differences do not exceed 10 cm s^{-1} in absolute value for the U component, whereas for the V component they fall in the range of $[-20, +12]$ cm s^{-1} (rms difference 3.8, 6.6 cm s^{-1} respectively).

Table 3 summarizes the tidal ellipse parameters for the major tides (K_1, M_2, S_2) and the dominant nontidal, low-frequency harmonic (MSf) derived from surface and moored current records. In the diurnal band, the dominant contribution associated with the K_1 harmonic (period of 23.93 h) shows a relatively large shear, coherently with a baroclinic mode of the water column and with diurnal sea-breeze wind forcing rather than the true tidal pattern for this frequency (Cosoli et al. 2005, 2008). A larger discrepancy is observed at a semidiurnal time scale (M_2, S_2 tides, periods of 12.42 and 12 h, respectively), but the differences in major and minor ellipse axes are comparable in size with their uncertainties. Phases and inclinations also differ but the mismatch between parameters is within the confidence level. Negligible differences are detected in ellipse parameters for the low-frequency MSf tide, except for a 4 cm s^{-1} difference in the ellipse major axis. Regardless, this difference is within the confidence level of the tidal parameter estimate.

7. Discussion

a. Radial and total currents

Currents in the area are weak because the typical values are comparable to their temporal variability and to the level of uncertainties of the radars reported by the manufacturer (nominal accuracy <7 cm s^{-1} in magnitude, 10° in direction; available online at http://www.codar.com/seasonde_specs.htm). Nevertheless, radar surface currents well captured the dominant spectral features of near-surface moored currents and tracked the general NE–SW average flow (Fig. 3; Cushman-Roisin et al. 2001; Kovačević et al. 2004). The comparison of surface current vectors and radial velocities with the current meter data at 2.5-m depth

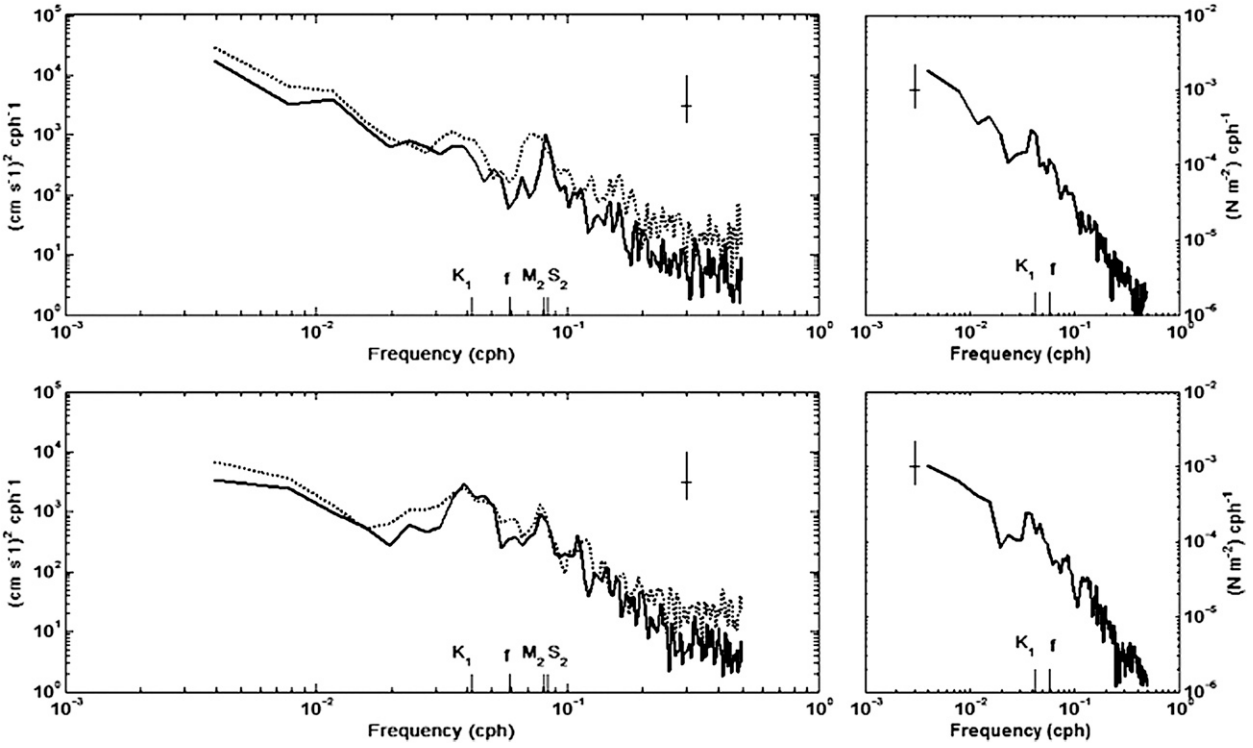

FIG. 5. (left) Cyclonic and anticyclonic components of rotary spectra for surface (dotted line) and subsurface currents for the level closer to the surface (solid line) are shown. (right) Cyclonic and anticyclonic portions of wind stress spectrum are shown. The dominant tidal harmonics and the local inertial frequencies are evidenced in the frequency axis. Units are in $(\text{cm s}^{-1})^2\ \text{cph}^{-1}$ and $(\text{N m}^{-2})^2\ \text{cph}^{-1}$ for currents and wind, respectively.

gave metrics (i.e., scalar and vector correlations, rms differences, mean biases, and bearing offsets) consistent with previously reported results for the area (Cosoli et al. 2005) for a 57.5-day deployment at a similar subsurface level (2.37-m depth) under a similar vertical stratification and wind regime. Metrics are also consistent with the typical values reported elsewhere (see, e.g., Emery et al. 2004). In general, the comparison statistics improved when the measured antenna beam pattern was used.

b. *Shallow-water effects*

HF SeaSonde radars operated in a relatively shallow coastal area, with depths in the range of 2–20 m in its

TABLE 3. Tidal ellipse parameters (major and minor axes, inclinations, phase angles) and their 95% confidence levels for surface radar currents and moored subsurface currents for the level closest to the surface for the low-frequency Msf, diurnal K_1, and semidiurnal M_2 and S_2 constituents.

Surface radar currents									
Tide	Frequency (cph)	Major (cm s^{-1})	Emajor (cm s^{-1})	Minor (cm s^{-1})	Eminor (cm s^{-1})	Inclination (°E)	Einclination (°E)	Phase angles (°)	Ephase angles (°)
MsF	0.002 821 9	9.4	6.5	0.6	3.2	78	17	214	37
K_1	0.041 780 7	5.1	1.2	−3.2	1.4	127	29	100	30
M_2	0.080 511 4	3.2	1.2	1.2	1.6	113	37	163	28
S_2	0.083 333 3	3.3	1.4	0.8	1.6	117	34	162	24
Moored subsurface currents									
MsF	0.002 821 9	13.7	8.8	0.6	2	77	7	220	34
K_1	0.041 780 7	3.8	1.4	−2.5	1.3	119	49	71	54
M_2	0.080 511 4	1.9	1.4	−1	1.9	13	110	309	71
S_2	0.083 333 3	2.4	1.4	−0.5	1.9	179	75	153	50

shallowest and deepest points, respectively. Water depth is a critical parameter because radial velocities are derived through the Doppler shift of the transmitted signal from gravity waves in their deep-water approximation: $H/L > 0.5$, where H is water depth and L the wavelength of the sea wave. Lipa et al. (2008) provide a detailed analysis of the effects of radar echoes returned from ocean waves that interact with the ocean floor, showing that shallow-water effects are most pronounced on the second-order spectra (i.e., waves) rather than on first order (i.e., ocean currents). The ocean waves required for the coherent Bragg scattering mechanism at the radar transmit frequencies (36, 25 MHz) have wavelengths of about 4 and 6 m, respectively; consequently, they satisfy the deep-water approximation in the major portion of the coverage area, in particular at the current meter mooring location (nominal depth 16 m). Moreover, shallow-water conditions are most likely to be met at locations close to shore where the intersection geometry is poor, the geometrical dilution of precision (GDOP; Chapman et al. 1997) is high, and the resulting total current vectors are discarded.

c. Velocity differences

Apart from the intrinsic differences related to the sampling strategies of radars versus current meters, differences between radar and subsurface records are also due to the geophysical variability within the water column (i.e., wind-driven or density-driven vertical current shears) or depend on measurement errors resulting from instrumental noise (Chapman et al. 1997). Graber et al. (1997) estimated that a combined effect of Ekman flow, Stokes drift, and baroclinic currents explained up to 22% of the rms differences between surface currents and currents at 5-m depth. In the Santa Barbara channel, the wind-induced current shears are shown to explain 10%–24% of the rms differences between radar and moored current records at 8-m depth (Emery et al. 2004).

Given the seasonal density stratification and the variable wind regime in the Adriatic Sea, the geophysical variability is similarly expected to account for part of the differences between surface and subsurface currents in the study area. Nevertheless, the analysi. is limited to the wind-driven shear because of the lack of stratification data.

Winds at the tower showed a predominant diurnal-period sea-breeze variability, with sharp meteorological fronts showing a wind speed of up to 20 m s^{-1} (Fig. 6). The typical value (50th percentile) for current shear between ADCP cells at 2.5 and 5.0 m in the analysis period was 2.7×10^{-2} s^{-1}, with a maximum value of 1.15×10^{-1} s^{-1} occurring under rapidly varying wind conditions. Assuming a log-layer model for the near-surface wind-driven shear, and using the wind stress data from the wind record at the tower, the rms value for the velocity differences between the 0.5-m level sampled by the surface radar and the 2.5-m depth for the shallowest ADCP level was estimated as 3.26 cm s^{-1}. This value represents 27%, 37%, and 22% of the rms differences for Lido, Pellestrina, and the tower radars, respectively. Thus, a relatively large fraction of radial velocity differences are related to wind-induced shear as already evidenced at a level of total current vector (Cosoli et al. 2005).

d. Bearing offsets

DF radars such as the SeaSonde suffer from pointing errors, originating either from distortions in the antenna patterns (i.e., departures of the antenna elements from their theoretical gain and phase patterns) induced by electromagnetic coupling with metal objects in the antennas near field or from the incorrect phase calibration of the antenna elements. Pattern distortions create ambiguities because the antenna response at one given bearing is close to that at a different angle. Consequently, the multiple signal classification (MUSIC) algorithm (Schmidt 1986) may not find a proper solution for the direction of the arrival of the sea echo, so that the correct Doppler velocities are placed at wrong angular sectors, and rms bearing errors as high as 35° are potentially introduced (Barrick and Lipa 1986).

Both Pellestrina and the tower sites exhibited statistically significant offsets for the measured ($\Delta\theta = +6°$; $\Delta\theta = +10°$) and the ideal ($\Delta\theta = +9°$; $\Delta\theta = +11°$) patterns. On the contrary, no bearing offset was detected at Lido (measured pattern) or it was far from being statistically significant (ideal pattern). The large bearing offsets at the tower arise from pattern distortions, whereas a more accurate calibration and the stable environment explain the best performances at Lido. The tower radar was seriously affected by the metal structures surrounding the antenna, which changed in time because of oceanographic research activities carried out on site while the radar operated. Emery et al. (2004) related pointing errors in ideal pattern radials with incorrect phase calibration of the three-element receive antenna. Findings of the present work show that pointing errors also originate from the antenna pattern angular smoothing, usually performed with the aim of mitigating the effects of irregularities and bearing ambiguities on the MUSIC algorithm (de Paolo and Terrill 2007). To test the effects of different smoothing (0°–30° angular smoothing, 5° step) on pointing errors, the Lido and Pellestrina sites had their radial velocities reprocessed from the raw Doppler spectra data and compared to moored data. Results for both sites evidenced that the lowest bearing offset occurred with the unsmoothed pattern, whereas an oversmoothing of up to

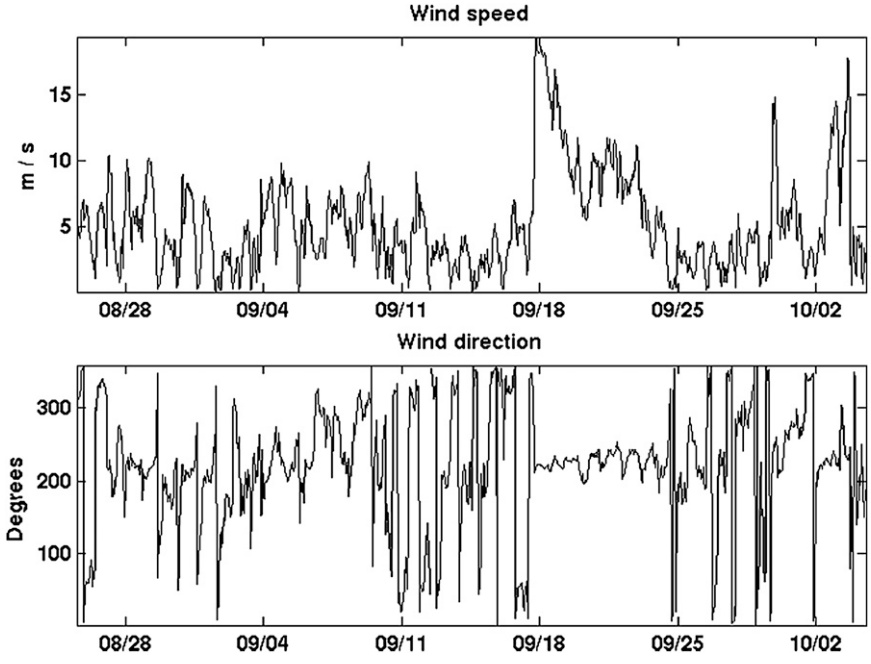

FIG. 6. Wind speed and direction at the oceanographic tower. Units are in m s^{-1} and degrees counterclockwise from the east.

30°, such that applied at Ptfv, resulted in the largest pointing errors.

Effects of bearing offsets on surface currents are expected to be minimal for Lido and Pellestrina. The horizontal separations between θ_{exp} and θ_{max} at these sites are lower than the decorrelation length scale of the flow in the area as derived from the observations. Also, the angular sectors that optimize the comparison statistics (θ_{max}) fall within the search radius used in the least squares approach. On the other hand, the combined effect of distance and nonzero $\Delta\theta$ [Eq. (2)] at the third site (Ptfv) might affect surface current accuracy. To test this hypothesis, the effects of bearing offsets on total currents were investigated with a simulation approach. An analytic flow field, defined over a regular grid, was decomposed into the corresponding radial fields for a three-site network similar to the experimental one. The radial maps were perturbed with a zero-mean Gaussian noise with a 2 cm s^{-1} standard deviation. Assuming in the first approximation that $\Delta\theta$ for each site is uniform over angle and range, bearing offsets were simulated as rigid rotations of the radial fields. Here, the unperturbed, the perturbed, and the rotated radial maps were then used to reconstruct the current field on the original grid. Error maps were finally derived as the difference between the original flow field and those reconstructed from the radial projections. Results for a purely zonal flow field evidenced that the effects of bearing offsets, evaluated at the mooring locations, biased the direction of the resulting current vector without affecting to a significant extent its magnitude. Regardless, this bias is within the noise level introduced in the total current vector by the least squares fit algorithm itself.

e. Radar coverage gaps and wind effects

Radar coverage at Lido and Pellestrina was stable over time and angle for both the ideal and the measured pattern, whereas the tower site presented a more heterogeneous spatial coverage with clustering of radial velocities over preferential bearing angles. A similar clustering is related to the antenna pattern distortions occurring at this station. All three sites had their maximum operating range set to 23 km, limited by the 200-kHz bandwidth at Pellestrina, and did not show any diurnal variability affecting HF radars operating at lower frequencies (Emery et al. 2004).

The time series of radial velocities presented gaps in time, the majority of which having a short (2–3 h) duration. Similar gaps originate from the MUSIC algorithm's inability to find a solution for a bearing angle at all times (Paduan and Rosenfeld 1996), poor signal-to-noise constraints for a Doppler line, or antenna pattern ambiguities (de Paolo and Terrill 2007). Gaps may also originate from the standard processing software provided by the manufacturer, which tends to exclude from the output those angular sectors with less than a predetermined number of radial velocities to provide

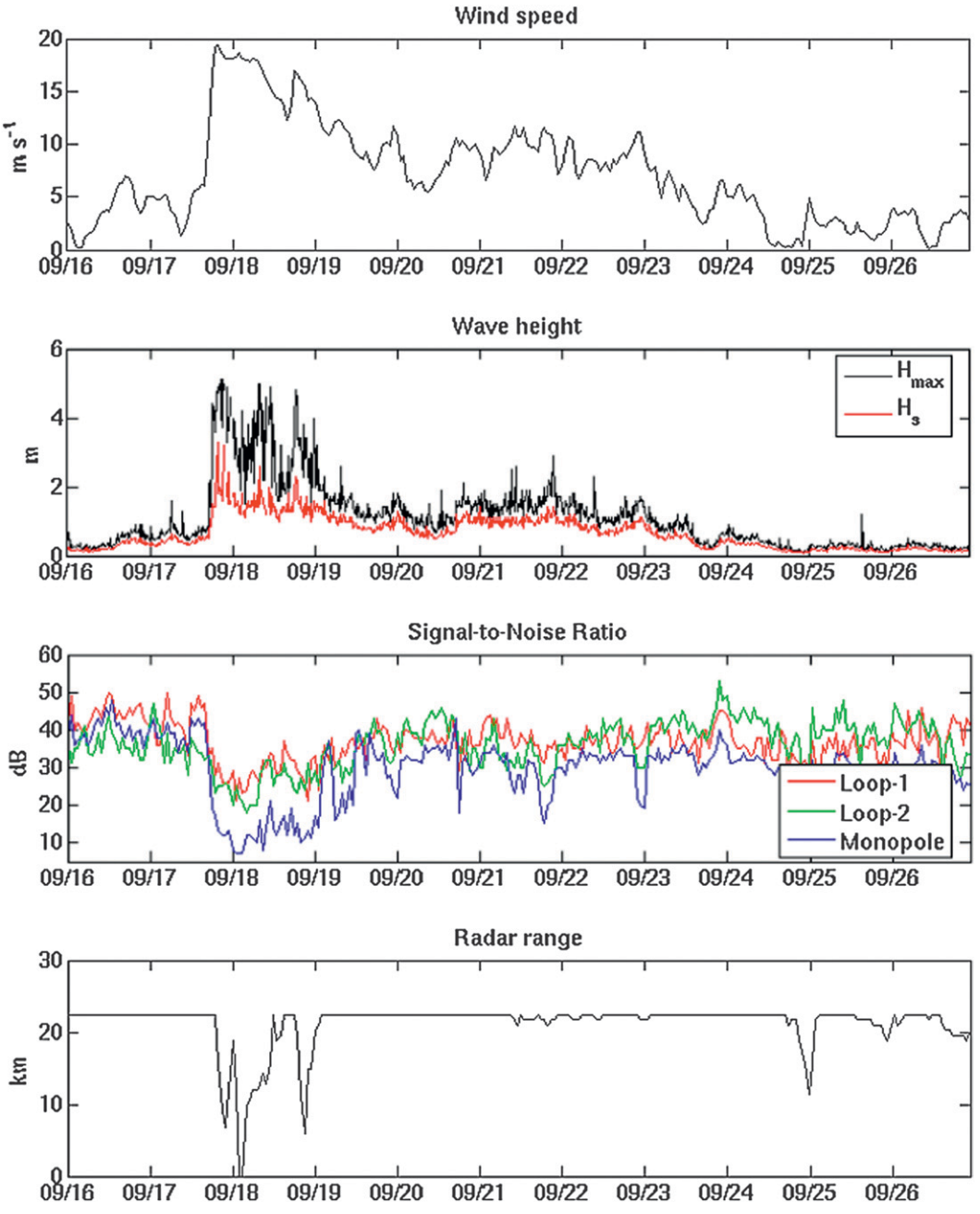

FIG. 7. Wind speed, maximum and significant wave height (H_m, H_s), signal-to-noise ratios at the receiver channel (loops and monopole), and radar operating range for the period of strong northeasterly wind.

statistical robustness to radial measurements. Longer gaps also occur, depending both on power supply outages (frequently occurring at the tower) and on adverse meteorological conditions. Although power supply–related problems are common to all installations, no report was found illustrating the effects of sudden wind bursts, such as those occurring in the Adriatic Sea, on HF radar performances. An example of coverage loss as wind turns on is presented in Fig. 7, where the noise level increases and the signal-to-noise ratios at the loops and monopole almost drop to zero. Waves up to 5–6-m maximum height (significant wave height 3 m) also build up with no lag to the wind pulse (Fig. 7). The range reduction with wind occurred simultaneously at the three sites independently of their operating frequency. Although the saturation limit for shallow water is less than the 6-m significant wave height for the 25-MHz band in deep-water conditions (Lipa et al. 2008), and waves in the area can be as high as

5–6 m, coverage loss appears to not be caused by saturation of the first-order Bragg region by the second-order echo spectrum. It rather appears as a broadband noise spanning the entire Doppler spectrum at all ranges, which masks the Bragg peaks and renders the extraction of radial velocities impossible. The causes of this coverage loss are still uncertain and more investigations are needed to understand the driving mechanism of similar failures. Similar episodes, frequently occurring in the area, significantly impact the measurements and determine gross underestimations (of up to 50%) of current amplitudes.

8. Conclusions

This works compares radar measurements of surface currents (measurement depth of 0.5 m) to subsurface currents recorded from an ADCP (measurement depth of 2.5 m) in the shallow coastal area offshore of the Venice lagoon, northern Adriatic Sea, for a 40-day period between August and October 2005. Results evidenced good correlations for radial velocities and for total vectors, with a general improvement for the calibrated pattern in comparison to the ideal one. Bearing offsets were present, originating from pattern distortions or pattern oversmoothing. These results support the importance of an accurate calibration of the antenna beam patterns and a proper choice of the operating parameters.

Wind-driven vertical shear within the water column accounted for a large fraction of differences between surface and subsurface currents. Bearing offsets also contributed to differences at a level of radial velocities, but their effects on surface current accuracy, evaluated with a simulated flow field, were negligible regardless of and comparable with the noise level intrinsic to the least squares method itself.

The radar operating range was stable, although with sporadic interruptions presumably related to limitations in the MUSIC algorithm, power interruptions or pattern distortions, the introduced short-duration gaps in time and space, or the determined radial velocity clustering over preferential directions.

Severe wind pulses were responsible for gaps and significant reductions in range, occurring simultaneously at the three stations independently of their operating frequencies. Similar events determined gross underestimations of current speed (up to 50% in magnitude) and need more detailed investigations given their influence on measurement accuracy.

Acknowledgments. This work was supported by CORILA (Consortium for the Coordination of the Scientific Research of the Venice Lagoon) within the three-year Research Program 2004–06.

REFERENCES

Barrick, D. E., and B. J. Lipa, 1986: Correcting for distorted antenna patterns in CODAR ocean surface measurements. *IEEE J. Oceanic Eng.,* **11,** 304–309.

Bergamasco, A., M. Gačić, R. Boscolo, and G. Umgiesser, 1996: Winter oceanographic conditions and water mass balance in the Northern Adriatic (February 1993). *J. Mar. Res.,* **7,** 67–94.

Cavaleri, L., S. Curiotto, A. Mazzoldi, and M. Pavanati, 1997: Long-term directional wave recording in the Northern Adriatic Sea. *Nuovo Cimento,* **20C,** 103–110.

Chapman, R. D., L. K. Shay, H. C. Graber, J. B. Edson, A. Karachintsev, C. L. Trump, and D. B. Ross, 1997: On the accuracy of HF radar surface current measurements: Intercomparisons with ship-based sensors. *J. Geophys. Res.,* **102,** 18 737–18 748.

Cosoli, S., M. Gačić, and A. Mazzoldi, 2005: Comparison between HF radar current data and moored ADCP current meter. *Nuovo Cimento,* **28C,** doi:10.1393/ncc/i2005-10032-6.

——, ——, and ——, 2008: Variability of currents in front of the Venice Lagoon, Northern Adriatic Sea. *Ann. Geophys.,* **26,** 1–16.

Cushman-Roisin, B. M. Gačić, P. M. Poulain, and A. Artegiani, Eds., 2001: *Physical Oceanography of The Adriatic Sea*. Kluver Academic Publishers, 304 pp.

de Paolo, T., and E. Terrill, 2007: Skill assessment of resolving ocean surface current structure using compact antenna style HF radar and the MUSIC direction finding algorithm. *J. Atmos. Oceanic Technol.,* **24,** 1277–1300.

Emery, B. M., L. Washburn, and J. A. Harlan, 2004: Evaluating radial current measurements from CODAR high-frequency radars with moored current meters. *J. Atmos. Oceanic Technol.,* **21,** 1259–1271.

Gačić, M., I. Mancero Mosquera, V. Kovačević, A. Mazzoldi, V. Cardin, F. Arena, and G. Gelsi, 2004: Temporal variations of water flow between the Venetian Lagoon and the open sea. *J. Mar. Syst.,* **51,** 33–47.

——, V. Kovačević, S. Cosoli, A. Mazzoldi, J. D. Paduan, I. Mancero Mosquera, and S. Yari, 2009: Surface current patterns in front of the Venice Lagoon. *Estuarine Coast. Shelf Sci.,* **82,** 485–494.

Graber, H. C., B. K. Haus, R. D. Chapman, and L. K. Shay, 1997: HF radar comparisons with moored estimates of current speed and direction: Expected differences and implications. *J. Geophys. Res.,* **102,** 18 749–18 766.

Gurgel, K. W., 1994: Shipborne measurements of surface current fields by HF radars. *L'onde Electrique,* **74,** 54–59.

Kovačević, V., M. Gačić, I. Mancero-Mosquera, A. Mazzoldi, and S. Marinetti, 2004: HF radar observations in the northern Adriatic: Surface current field in front of the Venetian Lagoon. *J. Mar. Syst.,* **51,** 95–122.

Large, W. G., and S. Pond, 1981: Open ocean momentum flux measurements in moderate to strong winds. *J. Phys. Oceanogr.,* **11,** 324–336.

Lipa, B., B. Nyden, D. Barrick, and J. Kohut, 2008: HF radar sea-echo from shallow water. *Sensors,* **8,** 4611–4635, doi:10.3390/s8084611.

Paduan, J. D., and L. K. Rosenfeld, 1996: Remotely sensed surface currents in Monterey Bay from shore-based HF radar (Coastal Ocean Dynamics Application Radar). *J. Geophys. Res.,* **101,** 20 669–20 686.

Schmidt, R. O., 1986: Multiple emitter location and signal parameter estimation. *IEEE Trans. Antennas Propag.,* **34,** 276–280.